

Nanographenes

Electronic Control of the Scholl Reaction: Selective Synthesis of Spiro vs Helical Nanographenes

Patricia Izquierdo-García, Jesús M. Fernández-García, Josefina Perles, Israel Fernández,* and Nazario Martín*

Dedicated to Professor Enrique Ortí on the occasion of his 65th birthday

Abstract: Scholl oxidation has become an essential reaction in the bottom-up synthesis of molecular nanographenes. Herein, we describe a Scholl reaction controlled by the electronic effects on the starting substrate (**1a,b**). Anthracene-based polyphenylenes lead to spiro-nanographenes under Scholl conditions. In contrast, an electron-deficient anthracene substrate affords a helically arranged molecular nanographene formed by two orthogonal dibenzo[fg,ij]phenanthro-[9,10,1,2,3-pqrst]pentaphene (DBPP) moieties linked through an octafluoroanthracene core. Density Functional Theory (DFT) calculations predict that electronic effects control either the first formation of spirocycles and subsequent Scholl reaction to form spironanographene **2**, or the expected dehydrogenation reaction leading solely to the helical nanographene **3**. The crystal structures of four of the new spiro compounds (*syn 2*, *syn 9*, *anti 9* and *syn 10*) were solved by single crystal X-ray diffraction. The photophysical properties of the new molecular nanographene **3** reveal a remarkable dual fluorescent emission.

Introduction

Nanographenes (NGs) are nano-sized fragments of 2D graphene with an open band gap^[1] (compared to the zero band gap of pristine graphene) due to the quantum effect of electronic confinement^[2] and/or the edge effects^[3] of these polycyclic aromatic hydrocarbons. The semiconducting nature derived from the separation between the valence and the conduction bands leads to optoelectronic properties^[4] entailing a growing number of cutting-edge applications, namely energy storage,^[5] sensors,^[6] molecular electronics^[7] or photovoltaics.^[8]

The monodisperse preparation of structurally well-defined molecular nanographenes with finely tuneable properties is accomplished through a bottom-up synthetic approach involving stepwise organic reactions.^[9] In the last decade, a great number of synthetic methodologies have been developed for the benchtop preparation of molecular NGs.^[10] The large majority of these synthetic strategies are based on the graphitization of polyphenylene intermediates mostly prepared by cross-coupling reactions,^[11] [4+2] cycloaddition^[12] or cyclotrimerization of aromatic alkynes.^[13]

One of the most widely extended and efficient methodologies for the graphitization of polyphenylenes is the Scholl oxidation, an intramolecular cyclodehydrogenative aryl-aryl coupling firstly reported by Roland Scholl in 1912.^[14] This oxidative formation of C–C covalent bonds between two unfunctionalized aryl moieties requires strong acidic conditions and an oxidant. The most frequent reagents to perform this transformation are FeCl₃ (that plays both roles of Lewis acid and oxidant) and dichlorodicyano-*p*-benzoquinone (DDQ) with a Brønsted acid such as triflic acid. Both experimental conditions are the most broadly and successfully used in the synthesis of nanographenes and allow the preparation of structures with a great variety of sizes and shapes, namely planar,^[15] curved^[16] and helical molecular nanographenes.^[17]

Understanding the mechanism of the Scholl reaction has been, and still is, a subject of study from both experimental^[18] and theoretical^[19] points of view. This transformation can proceed via two possible pathways involving either radical cation or arenium cation intermediates. The difficulty encountered in establishing the operating mechanism, which greatly depends on the electronic effects of the substrate and/or the nature of the reagents,^[20] makes the Scholl reaction become unpredictable sometimes, affording

[*] P. Izquierdo-García, Dr. J. M. Fernández-García, Dr. I. Fernández, Prof. Dr. N. Martín
 Departamento de Química Orgánica I, Facultad de Ciencias Químicas, Universidad Complutense de Madrid
 Avd. de la Complutense, S/N, 28040 Madrid (Spain)
 E-mail: nazmar@ucm.es
 israel@ucm.es

Dr. J. Perles
 Laboratorio de Difracción de Rayos X de Monocristal, SIdI, Universidad Autónoma de Madrid
 c/Francisco Tomás y Valiente, 7 Campus de Cantoblanco, 28049 Madrid (Spain)

Prof. Dr. N. Martín
 IMDEA-Nanociencia
 C/Faraday, 9, Campus de Cantoblanco, 28049 Madrid (Spain)

© 2022 The Authors. Angewandte Chemie International Edition published by Wiley-VCH GmbH. This is an open access article under the terms of the Creative Commons Attribution Non-Commercial License, which permits use, distribution and reproduction in any medium, provided the original work is properly cited and is not used for commercial purposes.

unexpected products resulting from rearrangements,^[21] undesired cyclizations^[22] or cation stabilities.^[23]

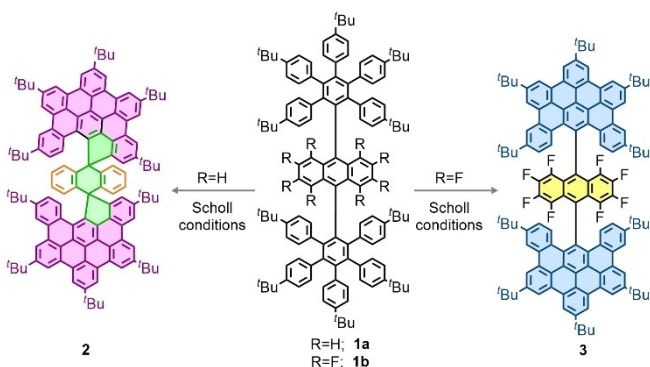
Despite this unpredictability, some methods to control the outcome of the Scholl reaction have been described in the literature. The suitable selection of the reaction conditions such as temperature,^[24] oxidant,^[25] Brønsted acid,^[26] Lewis acid^[27] and substrate^[28] allows directing the Scholl reaction to the formation of the target products.

Herein, we describe a Scholl reaction controlled by the electronic nature of the substrate (Scheme 1). On one hand, the anthracene-based polyphenylene **1a** (R=H) under Scholl conditions leads to the unexpected formation of a spironanographene *syn* **2**. To the best of our knowledge, the formation of spironanographenes has barely been described in the literature.^[29] Actually, in most cases, the formation of spirocycles occurs with concomitant rearrangements^[21b] or with the interruption of the graphitization process.^[21a] In our case, we take advantage of the presence of an anthracene-based architecture in our precursors to report the first example of spirocycles formation under the Scholl reaction conditions without interrupting the graphitization process. On the other hand, the use of the electron-deficient anthracene-based polyphenylene **1b** (R=F) leads to the formation of the expected graphitized helical molecular nanographene **3**. Furthermore, Density Functional Theory (DFT) calculations were carried out to rationalize the different chemical reactivity undergone by compounds **1a** and **1b**.

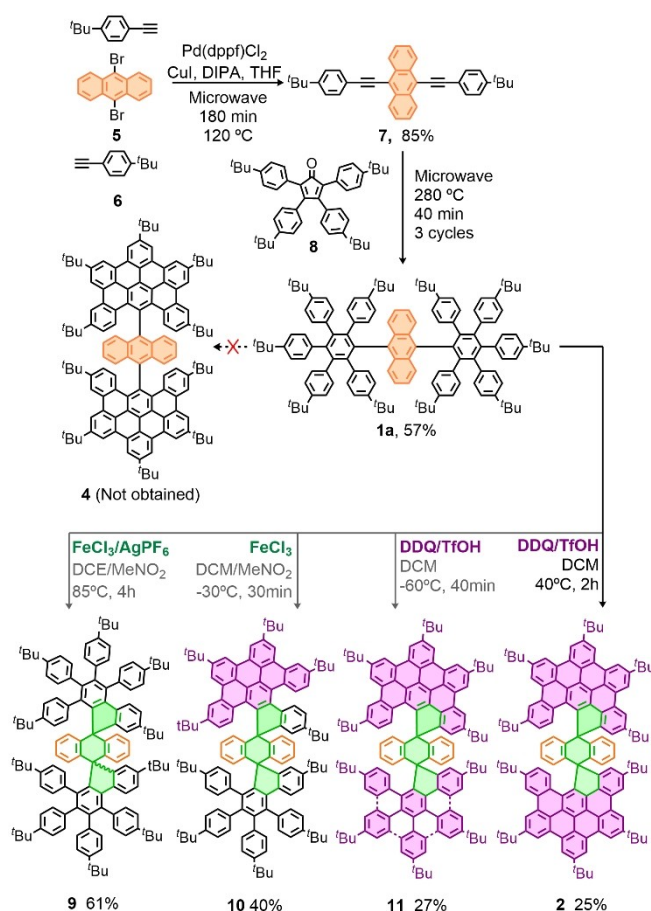
The electrochemical and photophysical absorption and emission properties of the new spironanographene **2** as well as the electron-deficient molecular nanographene **3** complement the synthetic and crystallographic (X-Ray) studies.

Results and Discussion

In this work, we firstly proposed the hypothetical synthesis of the eventually not obtained helically arranged molecular nanographene^[30] **4** (Scheme 2) based on a 9,10-substituted anthracene endowed with two dibenzo[fg,ij]phenanthro[9,10,1,2,3-pqrst]pentaphene (DBPP) units.



Scheme 1. Scholl oxidation of **1** leads to the formation of spironanographene *syn* **2** or helical nanographene **3** depending on the electronic features of the starting polyphenylene (**1a** or **1b**).



Scheme 2. Synthetic scheme for the synthesis of **1a** and further Scholl reaction. Depending on the reaction conditions, an isomeric mixture of spirocompounds **9** and **10** was isolated using FeCl₃ as an oxidant, or a more graphitized isomeric mixture of **11** (dashed lines in compound **11** indicates that one of these bonds is not formed) and *syn* **2** when DDQ was used as the oxidant reagent.

The first step of the synthetic methodology involved a double Sonogashira cross-coupling reaction between 9,10-dibromoanthracene **5** and two equivalents of 4-(*tert*-butyl)phenylacetylene **6**. The resulting compound, 9,10-bis-[(4-(*tert*-butyl)phenyl)ethynyl]anthracene **7**, was able to undergo a subsequent [4+2] cycloaddition reaction, followed by a two-fold CO extrusion using cyclopentadienone **8** as diene. The final step, the Scholl oxidation of polyphenylene **1a**, was expected to afford the final helical nanographene **4**. However, the formation of two spirocycles connecting the polyphenylene moieties to the central anthracene core was observed. During the optimization of the Scholl reaction conditions, partially graphitized intermediates **9**, **10** and **11**, as well as the fully-graphitized spironanographene **2**, were isolated.

On the one hand, FeCl₃ as an oxidant at 85 °C (interestingly, the use of relatively harsh conditions makes crucial the addition of a silver salt to prevent the formation of chlorinated products) led to an isomeric mixture of spirocompounds *syn* **9** and *anti* **9** where two spirocycles were formed without observing any graphitization of the poly-

phenylene moieties. The MALDI-ToF spectrum (Scheme S2, see Supporting Information) showed only one signal with molecular weight MW=1650, indicating the loss of two hydrogen atoms (**1a** MW=1652). Additionally, NMR experiments (Figure S4, see Supporting Information) revealed the presence of the two isomers and the formation of a sp^3 quaternary carbon at 63.8 ppm which corresponds to the spiranic carbon. Crystalline phases were obtained from the mixture of *syn* **9** and *anti* **9** and the two isomers were manually separated (see crystallographic section below). Moreover, $FeCl_3$ as an oxidant has also been employed at low temperature ($-30^\circ C$). Under these conditions, the reaction yielded a new isomeric mixture of **10** (Scheme 2). NMR experiments revealed the presence of two isomers and the MALDI-ToF spectrum showed only one signal corresponding to MW=1644 (Figure S5, see Supporting Information) that agrees with the loss of eight hydrogen atoms. As confirmed by single-crystal X-ray diffraction, *syn* **10** is a spirocompound partially graphitized with three new C–C bonds formed.

On the other hand, the use of DDQ as oxidant agent led to higher-graphitized compounds when compared to $FeCl_3$. In this way, a DDQ/TfOH mixture at $-60^\circ C$ generated a two-isomer mixture of **11**, in which the two spirocycles and seven (of eight possible) nanographene-like bonds were formed. NMR experiments showed the formation of a low-symmetry spirocompound where ten *tert*-butyl groups are observed for each isomer. Once again, MALDI-ToF shows a single signal with MW=1636 (Figure S6, see Supporting Information) that agrees with the formation of seven C–C bonds related to graphitization and two spirocycles. Finally, using DDQ as oxidant and raising the temperature to $40^\circ C$ affords the fully graphitized spironanographene *syn* **2** as the only isomer. MALDI-ToF spectrum showed one signal with MW=1634 indicating that the process occurred with total graphitization of the DBPPs moieties (Figure S2, see Supporting Information). 1H NMR spectrum of *syn* **2** (Figure S3, see Supporting Information) showed five *t*Bu groups, which agrees with a more symmetric structure. The signal at 69.9 ppm in the ^{13}C NMR spectrum revealed the presence of the sp^3 spiranic quaternary carbon atom. Moreover, the *syn* configuration was carefully assigned by 2D NMR (section 4, see Supporting Information) and confirmed by X-ray diffraction.

The crystal structures of four of the spirocompounds reported in this article, namely *syn* **2**, *syn* **9**, *anti* **9** and *syn* **10** (Figure 1) were solved by single crystal X-ray diffraction (section 5, see Supporting Information). They have been deposited at the CSD with numbers CCDC 2154765 (*syn* **9**) CCDC 2154766 (*anti* **9**), CCDC 2209634 (*syn* **10**) and CCDC 2209635 (*syn* **2**).

The two isomers of compound **9** could be manually separated from the crystallization mixture due to their different habits. Thus, crystals formed by the *syn* isomer adopt needle-like shapes, while those containing the *anti*-counterpart are ribbons.

Both crystallize in the triclinic *P*-1 space group with one molecule of **9** per asymmetric unit (Figures S28 and S30, see Supporting Information), as well as several disordered

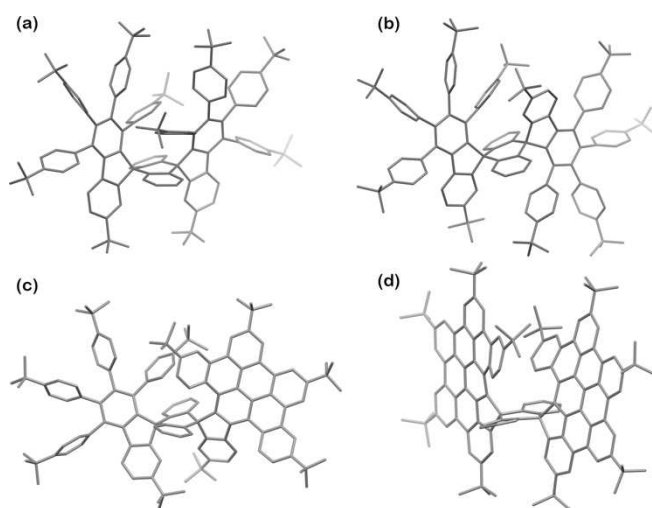


Figure 1. Molecular structure of the compounds solved by single crystal X-ray diffraction, where hydrogen atoms have been omitted for clarity; a) *syn* **9**, b) *anti* **9**, c) *syn* **10**, d) *syn* **2**.

solvent molecules. In both isomers, the two substituents around the anthracene core are located as separated as possible to avoid steric hindrance, resulting in similar lengths for *syn* and *anti* molecules (maximum distance between the pivotal carbon atoms of opposite *t*Bu groups C55–C111 in *syn* **9** of 20.426 Å; and C59–C115=21.525 Å in *anti* **9**), although the overall conformation of the two isomers is quite different. The lateral view of the *syn* isomer exhibits a V shape, with an angle between the side cores (defined by the central five- and the two six-membered rings at each side) of 18.35° while the *anti* isomer displays an H profile with a corresponding angle of 10.11° (Figure S39, a and b, see Supporting Information).

In both structural types, the packing is achieved by weak interactions, although the conformation of *anti* **9** allows stronger π - π and CH- π supramolecular bonds, which result in a more compact arrangement and, consequently, a smaller cell volume.

The molecular structure of one of the isomers of **10** was also solved. The molecule *syn* **10** is an intermediate between the spirocompound **9** and the spironanographene *syn* **2**, where one half of the molecule has undergone full oxidation to yield an aromatic layer, while the other half remains open. It crystallizes in the triclinic *P*-1 space group with one molecule per asymmetric unit (Figure S32, see Supporting Information). The lateral view of the core of this molecule shows an X-shaped profile, (Figure S39c, see Supporting Information) with an angle of 39.07° between the substituents around the anthracene core. Regarding its length, this species displays the highest value among the structures reported here, with a distance between C119–C55 Å carbon atoms of opposite *t*Bu groups of 22.166 Å.

It is remarkable that this molecule also exhibits the highest value of density among the structural types here presented, and no solvent molecules were found in the interstices. This is due to the effective CH- π supramolecular interactions that are formed between the hydrogen atoms

from *t*Bu groups in the open half of the molecule and the π systems in the aromatic side of neighbour ones.

Finally, single crystals were obtained for compound *syn* **2** and its crystal structure could also be solved. The nanographene molecules crystallize in the triclinic *P*-1 space group with one molecule per asymmetric unit (Figure S34, see Supporting Information) together with numerous disordered solvent molecules. In this case, the core of the molecule displays an H profile very similar to that found in *anti* **9**, with an angle of 10.86° (Figure S39d, see Supporting Information), and the longest distance found between opposite *t*Bu groups is 21.323 Å (C119–C59). The central parts of the nanographene layers are mostly parallel to each other, as can be seen in the packing of the molecules depicted in Figure S35 (see Supporting Information). The intramolecular CH- π bonds, together with the π - π interaction between the centroids of C49–C50 and C77–C82 (Figure 2a) bonds explain the torsion of the edges of the layers (Figures S36–S38, see Supporting Information), while the supramolecular CH- π contacts are responsible for the columnar packing found in the crystal of compound *syn* **2**. The occurrence of the intramolecular π - π and CH- π non-covalent interactions is further confirmed computationally by means of the NCIPLOT method on *syn* **2M**, a model system where the *t*Bu groups were replaced by methyl groups (see Figure 2b).

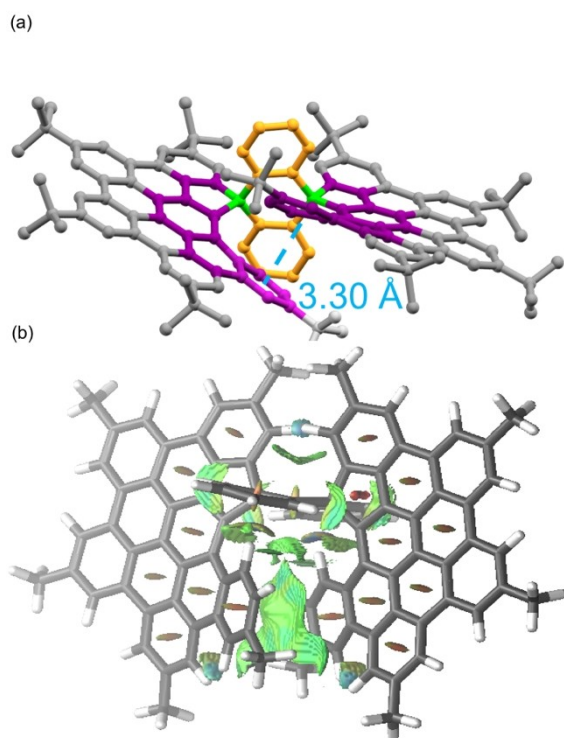


Figure 2. Intramolecular π - π interactions in *syn* **2**. a) X-ray structure. The blue dashed line represents the interaction between the centroids of C49–C50 and C77–C82. b) Contour plots of the reduced density gradient isosurfaces (density cutoff of 0.045 a.u.). The green surfaces indicate attractive non-covalent interactions.

The formation of partially graphitized spirocompounds **9**, **10** and **11**, and spironanographene *syn* **2** during Scholl cyclodehydrogenation suggests that the formation of the spirocycles occurs before the graphitization of the DBPPs moieties. To understand the unexpected formation of the spirocompound **2** at the expense of the non-spiranic expected product **4**, DFT calculations at the dispersion-corrected PCM(CH₂Cl₂)-B3LYP-D3/def2-SVP level were carried out.

Figure 3 shows the computed reaction profiles starting from the model anthracene derivative **1a-M** considering the two possible reaction mechanisms proposed for the Scholl reaction, i.e. the arenium cation and the radical cation pathways. For the arenium cation pathway, two possible carbocations can be formed upon reaction of the initial anthracene with the Scholl-reagents, namely the expected **INT1'** intermediate, where the protonation occurs at one of aryl groups attached to the central aryl group of the pentaaryl substituent, and intermediate **INT1**, where the protonation occurs directly at the anthracene core. Interestingly, our calculations indicate that the formation of **INT1** is strongly preferred ($\Delta\Delta G^\ddagger = 13.0$ kcal mol⁻¹) over the expected Scholl intermediate **INT1'**. In addition, the subsequent Scholl-cyclization reaction from **INT1'**, via transition state **TS1'**, is severely hampered in comparison to the alternative cyclization reaction from **INT1** (via **TS1**), from both kinetic ($\Delta\Delta G^\ddagger = 14.6$ kcal mol⁻¹) and thermodynamic ($\Delta\Delta G_R = 19.2$ kcal mol⁻¹) points of view. Therefore, it becomes evident that the reaction pathway leading to the observed spiranic compounds is clearly favored over the expected Scholl reaction along the entire reaction coordinate, which is fully consistent with the experimental findings.

Reasons for the enhanced stability of the initial intermediate **INT1** with respect to the Scholl intermediate **INT1'** can be mainly found in the aromaticity variation in the involved species. Indeed, the out-of-plane tensor component of the Nuclear Independent Chemical Shift (NICS) values,^[31] computed 1 Å above the ring centers, indicate that the aromaticity of the pendant aryl group in the initial reactant **1a-M** (NICS(1)_{zz} = -31.3 ppm) is dramatically reduced in the protonated intermediate **INT1'** (NICS(1)_{zz} = -13.4 ppm). At variance, the aromaticity of the adjacent aryl ring of the anthracene moiety (NICS(1)_{zz} = -22.4 ppm) is increased upon protonation of the central anthracene ring (NICS(1)_{zz} = -26.9 ppm). This aromaticity gain, which derives from the occurrence of a new Clar-sextet in the system,^[32] is translated into a significant thermodynamic stability and constitutes the driving force of the transformation. Therefore, **INT1** can be viewed as a highly stable trityl cation whose LUMO is mainly localized in the carbon atom bearing the positive charge and where the subsequent cyclization (via a standard S_EAr-type reaction) takes place (see inset in Figure 3).

Regarding the radical cation pathway, the initially formed intermediate **INT1-rad** strongly resembles the intermediate **INT1** formed in the arenium cation mechanism in the sense that the unpaired electron is mainly located exactly at the same anthracene carbon atom where the LUMO of **INT1** is centered (i.e. a trityl radical cation) and not at the

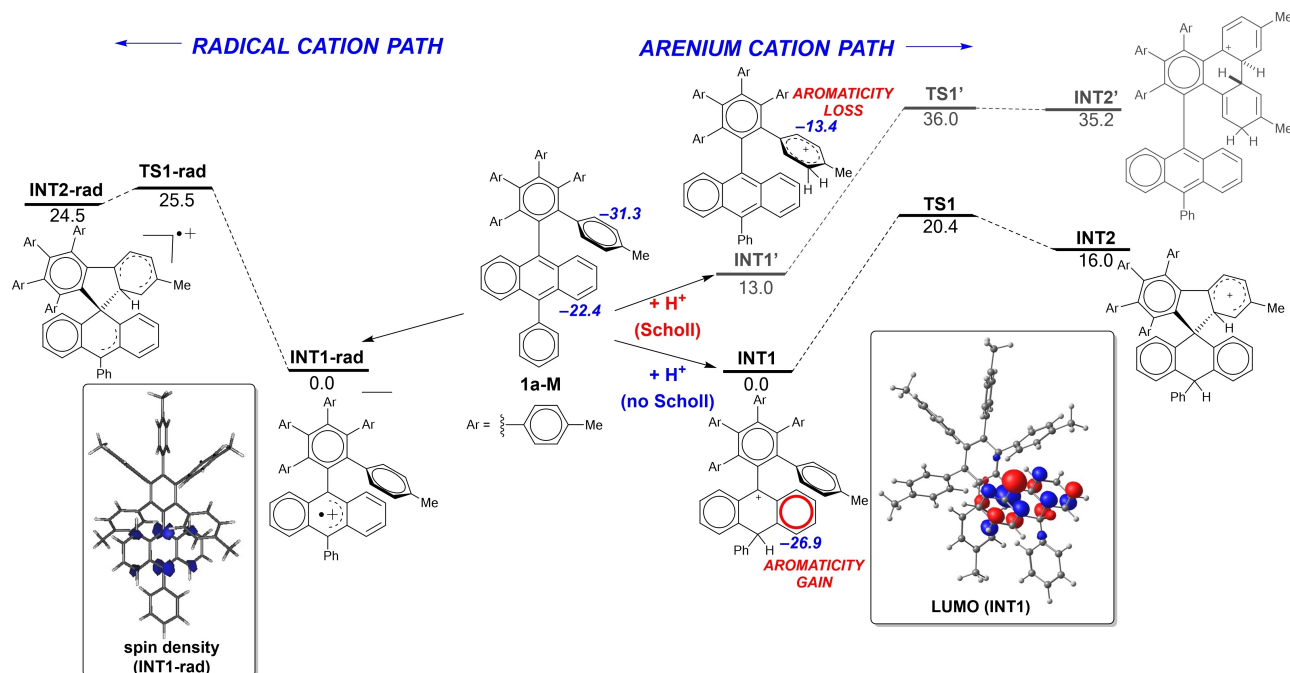
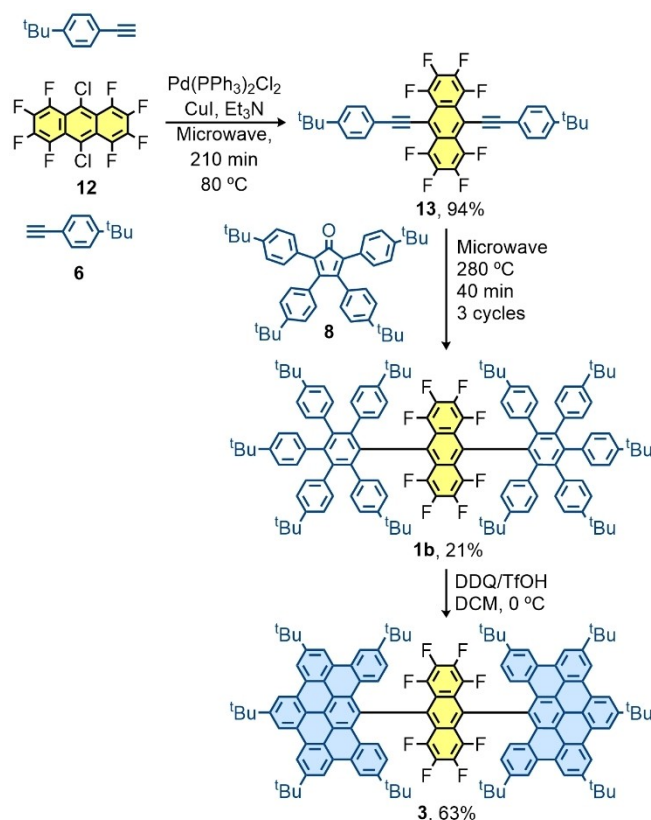


Figure 3. Computed reaction profiles for the Scholl and spiro-cyclization reactions involving anthracene derivative **1a-M**. Free energy values (ΔG , 298 K) are given in kcal mol⁻¹. Negative numbers in blue indicate the computed NICS(1)_{zz} values (in ppm). All data have been computed at the PCM(CH₂Cl₂)-B3LYP-D3/def2-SVP level. Inset: computed LUMO of intermediate **INT1** (isosurface value of 0.045 a.u.) and spin density of intermediate **INT1-rad** (isosurface value of 0.02 a.u.).

aryl groups of the pentaaryl substituent (see computed spin density in Figure 3). This involves that the subsequent cyclization reaction can only take place at this carbon atom leading exclusively to the corresponding spiranic species. Nevertheless, from the computed barrier and reaction energies, it can be concluded that the arenium cation pathway is favored over the alternative radical cation mechanism.

We hypothesized that the above-commented remarkable aromaticity increase ($\Delta\text{NICS}(1)_{zz} = 4.5$ ppm) when going from **1a-M** to **INT1** can be minimized by replacing the hydrogen atoms of the anthracene moiety with fluorine atoms. Strikingly, our NICS(1)_{zz} calculations on these systems indicate that the octafluorine-decorated **1b-M** is even more aromatic (-24.9 ppm) than the corresponding cationic species **INT1b** (-20.7 ppm). This suggests that going from **1b-M** to **INT1b** does not involve an aromaticity gain (as it occurred with its non-fluorinated counterpart **1a-M**) but an aromaticity loss ($\Delta\text{NICS}(1)_{zz} = -4.2$ ppm), which might switch off the preference for the spiro-cyclization pathway.

Encouraged by this result, we were prompted to prepare the octafluoroanthracene derivative **1b**, where the central anthracene core was endowed with eight electron-withdrawing fluorine atoms (Scheme 3). In a similar manner to that employed for the preparation of the spironanographene *syn* **2**, the synthesis started with a double Sonogashira coupling between 9,10-dichloro-1,2,3,4,5,6,7,8-octafluoroanthracene **12** and two equivalents of 4-(*tert*-butyl)phenylacetylene **6**. In this case, the use of an aryl



Scheme 3. Synthetic scheme for the preparation of nanographene **3**, where the electron-withdrawing effects of the F atoms control the fate of the Scholl reaction.

chloride instead of aryl bromide required different reaction conditions to prevent undesired alkyne homocoupling reactions. The resulting compound, 9,10-bis[(4-(*tert*-butyl)phenyl)ethynyl]-1,2,3,4,5,6,7,8-octafluoroanthracene **13** underwent a [4+2] cycloaddition with cyclopentadienone **8**, followed by CO extrusion. The final Scholl oxidation of polyphenylene **1b** using DDQ as oxidant afforded the final helically arranged nanographene **3**. In this case, the dehydrogenation process is controlled by the electronic properties of the fluorinated anthracene core and the graphitization of polyphenylene **1b** took place selectively without the formation of spirocycles.

Nanographene **3** was fully characterized by ^1H , ^{13}C , ^{19}F , FT-IR and high-resolution mass spectrometry. NMR spectra of **3** reveal only three *t*Bu groups with 2:2:1 relative intensities and two ^{19}F signals (Figure S10, see Supporting Information). These signals correspond to a quarter of the whole molecule, revealing the highly symmetric nature of this structure.

The electrochemical properties of nanographenes *syn 2* and **3** were explored by cyclic voltammetry in a toluene/acetonitrile 1:1 mixture with tetrabutylammonium hexafluorophosphate as supporting electrolyte and Ag/AgNO₃ as reference electrode at room temperature. Table 1 shows the reduction and oxidation potentials of *syn 2* and **3** vs Fc/Fc⁺ compared to those of hexa-*tert*-butylhexa-peri-hexabenzocoronene (*t*Bu-HBC). On the one hand, *syn 2* shows one quasireversible reduction potential at −2.56 V, indicating its poorer electron acceptor nature when compared to *t*Bu-HBC. The first quasireversible oxidation wave at 0.85 V shows also less donor behaviour than *t*Bu-HBC. These data reveal a higher band gap compared to *t*Bu-HBC, probably due to the presence of the *sp*³ spiranic carbons that interrupts the classical π -conjugation. On the other hand, the first quasireversible reduction potential of nanographene **3** at −1.69 V is significantly shifted to lower negative values, which reveals the better electron acceptor behaviour of **3** when compared to *t*Bu-HBC, due to the presence of the

electron-withdrawing octafluoroanthracene central moiety. Additionally, **3** shows three reduction potentials at −2.40, −2.47 and −2.69 V, whereby nanographene **3** is able to accept up to four electrons under these experimental conditions. The first quasireversible oxidation wave of **3** (0.87 V) shows a slightly lower trend to undergo oxidation reactions, compared to *t*Bu-HBC. This experimental finding could be accounted for by the lower conjugation of the π -system in **3**, as well as by the presence of the close fluorinated anthracene unit. The observed electrochemical trend nicely correlates with the DFT-computed energy of the corresponding LUMO (the orbital accepting the first electron upon electrochemical reduction) of **2M** and **3M** (model systems where the *t*Bu groups were replaced by methyl groups) as compared to HBC: −2.65 eV (**3M**) < −1.92 eV (HBC) < −1.71 eV (**2M**), thus showing that a more stabilized LUMO is translated into the observed lower reduction potentials.

The UV/Vis absorption and emission spectra of spirona-nanographene *syn 2* are shown in Figure 4 and Table 2. The absorption spectrum principally shows three sharp absorption bands (324, 336 and 350 nm) and two weak bands (276 and 391 nm) in the UV region. The vis region shows two very weak bands (414 and 438 nm). In comparison, the spectrum of *t*Bu-HBC shows a similar shape, with three sharp absorptions in the UV region (344, 360, and 390 nm) and weak bands in the vis region (439, 441, and 443 nm).^[16b] In agreement with the electrochemical data, the bands of

Table 1: Redox potentials of *t*Bu-HBC and nanographene **3** vs Fc/Fc⁺.^[a]

Compound	E^1_{red} [V]	E^2_{red} [V]	E^3_{red} [V]	E^4_{red} [V]	E^1_{ox} [V]
<i>t</i> Bu-HBC	−2.27	−2.50	−2.79	–	0.67
<i>syn 2</i>	−2.56	–	–	–	0.85
3	−1.69	−2.40	−2.47	−2.69	0.87

[a] Measurements carried out in toluene/acetonitrile 1:1 mixture at room temperature using tetrabutylammonium hexafluorophosphate as supporting electrolyte, a glassy carbon as working electrode, platinum wire as counterelectrode, and Ag/AgNO₃ as reference electrode.

Table 2: UV/Vis Absorption and Emission Bands of *t*Bu-HBC and **3**.^[a]

Compound	absorption $\lambda_{\text{abs}}^{\text{max}}$ [nm]	emission $\lambda_{\text{em}}^{\text{max}}$ [nm]
<i>t</i> Bu-HBC ^[b]	344, 360, 390, 439, 441, 443	493, 519, 553
<i>syn 2</i>	324, 336, 350, 376, 391, 414, 438	439, 456, 465, 484, 496
3	310, 337, 367, 381, 413, 454, 482	437, 454, 464, 499, 531, 575

[a] Measurements carried out in hexane at room temperature. [b] data extracted from ref. [16b].

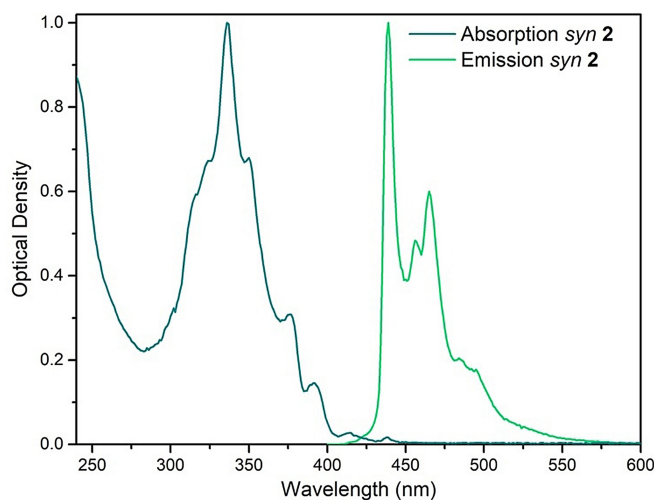


Figure 4. Normalized absorption (dark green) and emission (clear green) spectra of *syn 2* recorded in hexane at room temperature

nanographene **syn 2** are blue-shifted, with the subsequent increase of the band gap of the molecule.

The presence of the sp^3 carbon atoms in the spironanographene **syn 2** severely hampers the electronic communication (through bonds) between both π -extended fragments. This is confirmed by the visualization of the corresponding frontier molecular orbitals, which are π -delocalized orbitals centered in both π -extended moieties with no coefficients in the central anthracene core (Figure 5). This is also reflected

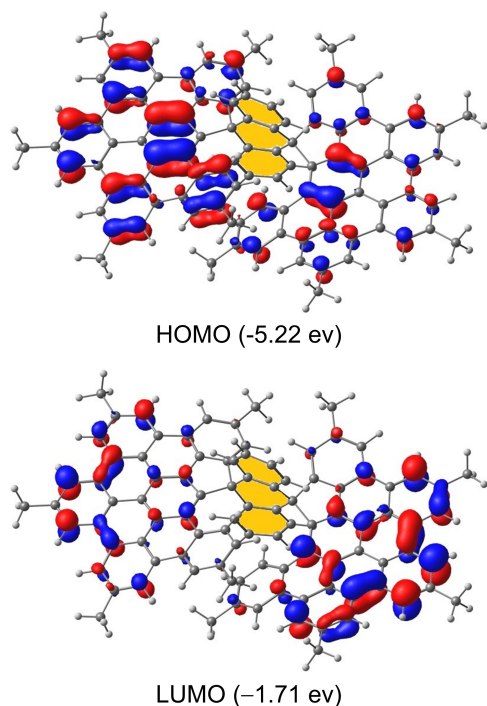


Figure 5. Computed frontier molecular orbitals HOMO (above) and LUMO (below) of **syn 2** using a model with ^tBu groups substituted by Me.

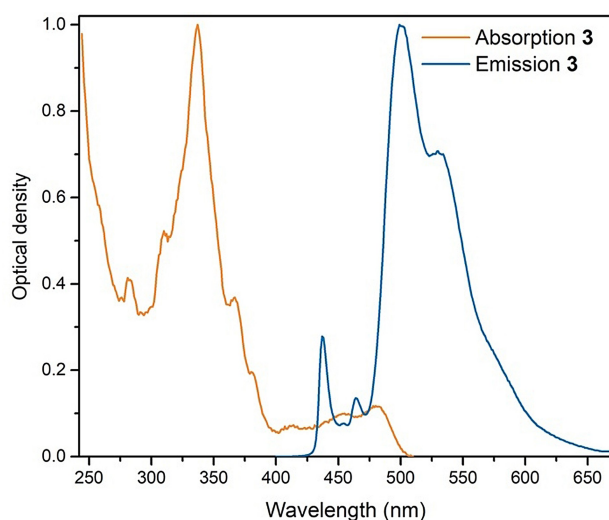


Figure 6. Normalized absorption (orange) and emission (blue) spectra of **3** recorded in hexane at room temperature

in the recorded UV/Vis which strongly resembles that of the HBC system with two rather low intensity bands at 414 and 438 nm, respectively. Our TD-DFT calculations indicate that these bands, having rather low oscillator strengths of 0.06 and 0.09, respectively, are the result of combinations of vertical transitions involving orbitals from HOMO-4 up to LUMO+3.

The emission spectrum of **syn 2** shows three sharp bands at 439, 456 and 464 nm and two less intense bands at 484 and 496 nm. Compared with ^tBu-HBC that shows a broad band at 493 nm with a shoulder at 553 nm, the bands of **syn 2** are more defined and sharpened.

The UV/Vis absorption and emission spectra of nanographene **3** are shown in Figure 6 and Table 2. The absorption spectrum shows three sharp absorption bands in the UV region (310, 337 and 367 nm) and three weak bands in the vis region (381, 454 and 482 nm). In comparison, the spectrum of ^tBu-HBC shows a similar shape, with three sharp absorptions in the UV region (344, 360, and 390 nm) and weak bands in the vis region (439, 441, and 443 nm).^[16b] In concordance with the electrochemical studies, the lower-energy bands in nanographene **3** are red-shifted, which is in agreement with the stabilization of the LUMO in **3** (see above), resulting in a significant decrease of the band gap of the molecule.

Time-dependent (TD)-DFT calculations were carried out to understand the nature of the red-shifted bands observed for nanographene **3**. Our PCM(hexane)-TD-B3LYP-D3/def2-SVP//B3LYP-D3/def2-SVP calculations on the model **3M** indicate that the absorption at ca. 500 nm can be assigned to the vertical transition involving the one-electron promotion from the HOMO to the LUMO. These orbitals can be viewed as π -molecular orbitals located mainly at the anthracene moiety (central and perfluorinated rings, respectively, Figure 7). This sharply contrasts with related systems involving C₆F₄ as the central core where the frontier molecular orbitals are delocalized mainly over the DBPP groups resulting in a higher energy transition ($\lambda = 444$ nm).^[29] Our calculations also show that the next band is associated with the HOMO-1→LUMO transition, being the HOMO-1 (which is nearly degenerate to the HOMO) a π -delocalized orbital centered in both pentaphene fragments (Figure 7).

On the other hand, the emission spectrum of **3** apparently reveals a dual emission corresponding to the two main fragments which constitute the molecule. Thus, nanographene **3** shows bands in the vis region, two weak sharp bands at 437 and 464 nm, together with other more intense broad bands located at 501, 531 and 575 nm. Interestingly, the weaker bands at 437, 454 and 464 nm can be reasonably assigned to the DBPP fragment resulting from the graphitization process that occurred in the Scholl reaction. As expected, the rest of the bands are, therefore, stemming from the octafluoroanthracene moiety that could be deduced by comparison with the shape of the emission spectra of the precursors **1b**, **12** and **13** (Figure S12, see Supporting Information).

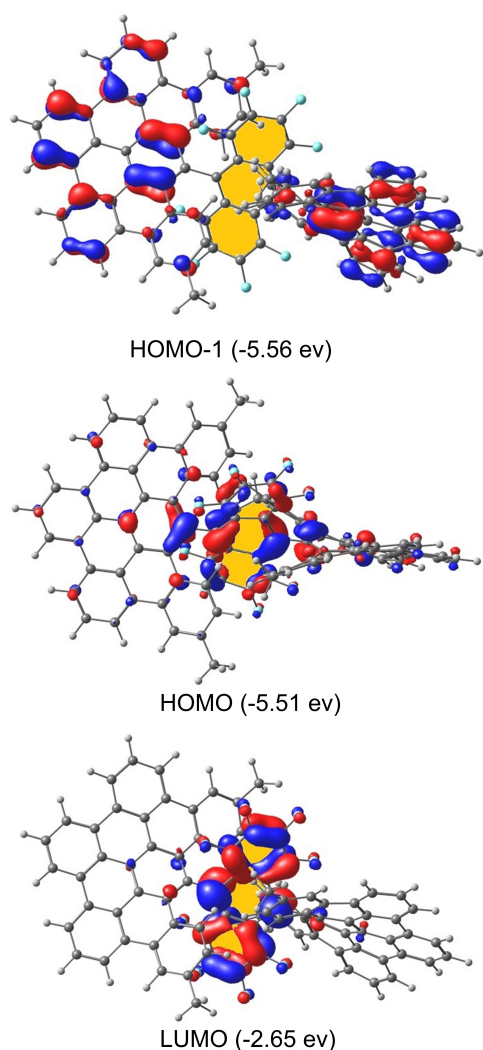


Figure 7. Computed molecular orbitals (isosurface value of 0.035 au) for nanographene **3M**.

Conclusion

In summary, a Scholl reaction controlled by the electronic effects of the starting substrate, namely anthracene versus octafluoroanthracene, is described.

Anthracene-based polyphenylene **1a**, without notorious electronic effects, leads to a series of spirocompounds **2**, **9**, **10** and **11** with a different degree of graphitization depending on the temperature, reaction time and oxidant used in the Scholl reaction. DFT calculations nicely explain the closure of the spirocycles. The formation of a highly stabilized trityl cation with a noticeable increment of the aromaticity of the anthracene moiety leads to the kinetically and thermodynamically favoured attack over the central ring of anthracene with the subsequent formation of the spirocompounds **2**, **9**, **10** and **11**. In contrast, when using a substrate endowed with electron-withdrawing groups -in order to destabilize the trityl cation- such as octafluoroanthracene-based polyphenylene **1b**, the Scholl reaction affords the expected helically arranged molecular nano-

graphene **3** in a graphitization process without the formation of any trace of the corresponding spirocycles.

Thus, it is shown how electronic effects can enable the graphitization toward the straightforward formation of spironanographenes, avoiding the formation of stabilized carbocations that disrupt the Scholl reaction.

The electrochemical and photophysical studies of the novel spironanographene *syn* **2** show the interruption of the electronic communication due to the formation of two sp^3 spiranic carbons. Its opened band gap (compared with HBC) is revealed by more separated reduction and oxidation potentials and its blue-shifted electronic bands. Helically arranged nanographene **3** shows its acceptor character with a comparatively lower first reduction potential in the CV, and red-shifted bands in the absorption and emission spectra. Additionally, **3** shows a dual emission with separated bands stemming from the octafluoroanthracene fragment and the DBPP moieties. In this regard, the nanographene now reported is an interesting candidate to determine its photophysical properties -as a proof of concept- in the search for new carbon-based models where the orthogonal arrangement of the frontier orbitals could lead to the observation of Thermally Activated Delayed Fluorescence (TADF), thus paving the way to the search for optoelectronic applications. In this regard, work is currently in progress in our research group.

Acknowledgements

Financial support from the Spanish MICINN (Projects PID2020-114653RB-I00 and RED2018-102815-T to N.M. and PID2019-106184GB-I00 and RED2018-102387-T to I.F.) is acknowledged. J. Perles wishes to thank Dr. Jakub M. Wojciechowski for the data collection of compound **10**, and Dr. Mario Ramírez for his help with the molecular models.

Conflict of Interest

The authors declare no conflict of interest.

Data Availability Statement

Research data are not shared.

Keywords: DFT Calculations • Helically Arranged Nanographenes • Molecular Nanographenes • Scholl Reaction • Spironanographenes

- [1] a) S. Y. Zhou, G. H. Gweon, A. V. Fedorov, P. N. First, W. A. De Heer, D. H. Lee, F. Guinea, A. H. Castro Neto, A. Lanzara, *Nat. Mater.* **2007**, *6*, 770; b) R. Balog, B. Jorgensen, L. Nilsson, M. Andersen, E. Rienks, M. Bianchi, M. Fanetti, E. Laegsgaard, A. Baraldi, S. Lizzit, Z. Sljivancanin, F. Besenbacher, B. Hammer, T. G. Pedersen, P. Hofmann, L. Horne-

- kaer, *Nat. Mater.* **2010**, 9, 315; c) M. Dvorak, W. Oswald, Z. G. Wu, *Sci. Rep.* **2013**, 3, 2289; d) T. Zhao, C. Xu, W. Ma, Z. B. Liu, T. Y. Zhou, Z. Liu, S. Feng, M. J. Zhu, N. Kang, D. M. Sun, H. M. Cheng, W. C. Ren, *Nat. Commun.* **2019**, 10, 4854.
- [2] a) M. Vázquez-Nakagawa, L. Rodríguez-Pérez, M. Á. Herranz, N. Martín, *Chem. Commun.* **2016**, 52, 665; b) C. I. M. Santos, L. Rodríguez-Pérez, G. Gonçalves, S. N. Pinto, M. Melle-Franco, P. A. A. P. Marques, M. A. F. Faustino, M. A. Herranz, N. Martín, M. G. P. M. S. Neves, J. M. G. Martinho, E. M. S. Maçôas, *Carbon* **2020**, 166, 164; c) Y. R. Kumar, K. Deshmukh, K. K. Sadasivuni, S. K. K. Pasha, *RSC Adv.* **2020**, 10, 23861; d) S.-Y. Li, L. He, *Front. Phys.* **2021**, 17, 33200.
- [3] a) S. Fujii, T. Enoki, *Acc. Chem. Res.* **2013**, 46, 2202; b) Y. Gu, X. Wu, T. Y. Gopalakrishna, H. Phan, J. Wu, *Angew. Chem. Int. Ed.* **2018**, 57, 6541; *Angew. Chem.* **2018**, 130, 6651; c) J. Liu, X. Feng, *Angew. Chem. Int. Ed.* **2020**, 59, 23386; *Angew. Chem.* **2020**, 132, 23591.
- [4] a) J. Wu, W. Pisula, K. Müllen, *Chem. Rev.* **2007**, 107, 718; b) F. Bonaccorso, Z. Sun, T. Hasan, A. C. Ferrari, *Nat. Photonics* **2010**, 4, 611; c) C. Wang, H. Dong, W. Hu, Y. Liu, D. Zhu, *Chem. Rev.* **2012**, 112, 2208; d) A. Ambrosi, C. K. Chua, A. Bonanni, M. Pumera, *Chem. Rev.* **2014**, 114, 7150; e) R. M. Metzger, *Chem. Rev.* **2015**, 115, 5056; f) N. Martín, *Adv. Energy Mater.* **2017**, 7, 161102; g) Z. Sun, S. Fang, Y. H. Hu, *Chem. Rev.* **2020**, 120, 10336.
- [5] a) Z. Zhou, X.-Y. Wang, Z. Wei, K. Müllen, M. A. Petrukhina, *Angew. Chem. Int. Ed.* **2019**, 58, 14969; *Angew. Chem.* **2019**, 131, 15111; b) Z. Zhou, L. Fu, Y. Hu, X.-Y. Wang, Z. Wei, A. Narita, K. Müllen, M. A. Petrukhina, *Angew. Chem. Int. Ed.* **2020**, 59, 15923; *Angew. Chem.* **2020**, 132, 16057; c) Y. Zhang, Y. Zhu, D. Lan, S. H. Pun, Z. Zhou, Z. Wei, Y. Wang, H. K. Lee, C. Lin, J. Wang, M. A. Petrukhina, Q. Li, Q. Miao, *J. Am. Chem. Soc.* **2021**, 143, 5231; d) Z. Zhou, Z. Wei, K. Ikemoto, S. Sato, H. Isobe, M. A. Petrukhina, *Angew. Chem. Int. Ed.* **2021**, 60, 11201; *Angew. Chem.* **2021**, 133, 11301; e) S. N. Spisak, Z. Zhou, S. Liu, Q. Xu, Z. Wei, K. Kato, Y. Segawa, K. Itami, A. Yu. Rogachev, M. A. Petrukhina, *Angew. Chem. Int. Ed.* **2021**, 60, 25445; *Angew. Chem.* **2021**, 133, 25649; f) Z. Zhou, J. M. Fernández-García, Y. Zhu, P. J. Evans, R. Rodríguez, J. Crassous, Z. Wei, I. Fernández, M. A. Petrukhina, N. Martín, *Angew. Chem. Int. Ed.* **2022**, 61, e202115747; *Angew. Chem.* **2022**, 134, e202115747; g) Z. Zhou, Y. Zhu, J. M. Fernández-García, Z. Wei, I. Fernández, M. A. Petrukhina, N. Martín, *Chem. Commun.* **2022**, 58, 5574.
- [6] a) N. Panwar, A. M. Soehartono, K. K. Chan, S. Zeng, G. Xu, J. Qu, P. Coquet, K. T. Yong, X. Chen, *Chem. Rev.* **2019**, 119, 9559; b) E. Jin, Q. Yang, C. W. Ju, Q. Chen, K. Landfester, M. Bonn, K. Müllen, X. Liu, A. Narita, *J. Am. Chem. Soc.* **2021**, 143, 10403.
- [7] a) S. Mishra, D. Beyer, K. Eimre, S. Kezilebieke, R. Berger, O. Groning, C. A. Pignedoli, K. Müllen, P. Liljeroth, P. Ruffieux, X. Feng, R. Fasel, *Nat. Nanotechnol.* **2020**, 15, 22; b) L. Đorđević, C. Valentini, N. Demitri, C. Mézière, M. Allain, M. Sallé, A. Folli, D. Murphy, S. Mañas-Valero, E. Coronado, D. Bonifazi, *Angew. Chem. Int. Ed.* **2020**, 59, 4106; *Angew. Chem.* **2020**, 132, 4135; c) S. Zank, J. M. Fernández-García, A. Stasyuk, A. Voityuk, M. Krug, M. Solà, D. Guldi, N. Martín, *Angew. Chem. Int. Ed.* **2022**, 61, e202112834; *Angew. Chem.* **2022**, 134, e202112834.
- [8] a) J. Cao, Y. M. Liu, X. Jing, J. Yin, J. Li, B. Xu, Y. Z. Tan, N. Zheng, *J. Am. Chem. Soc.* **2015**, 137, 10914; b) N. Martín, *Adv. Energy Mater.* **2017**, 7, 1601102; c) J. Urieta-Mora, I. García-Benito, A. Molina-Ontoria, N. Martín, *Chem. Soc. Rev.* **2018**, 47, 8541.
- [9] a) F. Mercuri, M. Baldoni, A. Sgamellotti, *Nanoscale* **2012**, 4, 369; b) J. M. Tour, *Chem. Mater.* **2014**, 26, 163; c) M. Bacon, S. J. Bradley, T. Nann, *Part. Part. Syst. Charact.* **2014**, 31, 415.
- [10] a) H. Ito, K. Ozaki, K. Itami, *Angew. Chem. Int. Ed.* **2017**, 56, 11144; *Angew. Chem.* **2017**, 129, 11296; b) J. M. Fernández-García, P. J. Evans, S. Filippone, M. A. Herranz, N. Martín, *Acc. Chem. Res.* **2019**, 52, 1565; c) H. Ito, Y. Segawa, K. Murakami, K. Itami, *J. Am. Chem. Soc.* **2019**, 141, 3; d) I. A. Stepek, K. Itami, *ACS Mater. Lett.* **2020**, 2, 951; e) W. Matsuoka, H. Ito, D. Sarlah, K. Itami, *Nat. Commun.* **2021**, 12, 3940; f) J. M. Fernández-García, P. Izquierdo-García, M. Buendía, S. Filippone, N. Martín, *Chem. Commun.* **2022**, 58, 2634.
- [11] a) D. Lungerich, D. Reger, H. Holzel, R. Riedel, M. M. Martin, F. Hampel, N. Jux, *Angew. Chem. Int. Ed.* **2016**, 55, 5602; *Angew. Chem.* **2016**, 128, 5692; b) W. Haguí, H. Doucet, J.-F. Soulé, *Chem* **2019**, 5, 2006.
- [12] a) I. C.-Y. Hou, Y. Hu, A. Narita, K. Müllen, *Polym. J.* **2018**, 50, 3; b) K. P. Kawahara, W. Matsuoka, H. Ito, K. Itami, *Angew. Chem. Int. Ed.* **2020**, 59, 6383; *Angew. Chem.* **2020**, 132, 6445; c) X. Zhang, M. R. Mackinnon, G. J. Bodwell, S. Ito, *Angew. Chem. Int. Ed.* **2022**, 61, e202116585; *Angew. Chem.* **2022**, 134, e202116585.
- [13] a) T. Jin, J. Zhao, N. Asao, Y. Yamamoto, *Chem. Eur. J.* **2014**, 20, 3554; b) I. Pozo, E. Guitián, D. Perez, D. Pena, *Acc. Chem. Res.* **2019**, 52, 2472; c) W. J. Kong, L. H. Finger, J. C. A. Oliveira, L. Ackermann, *Angew. Chem. Int. Ed.* **2019**, 58, 6342; *Angew. Chem.* **2019**, 131, 6408; d) A. Yubuta, T. Hosokawa, M. Gon, K. Tanaka, Y. Chujo, A. Tsurusaki, K. Kamikawa, *J. Am. Chem. Soc.* **2020**, 142, 10025.
- [14] a) R. Scholl, C. Seer, *Justus Liebigs Ann. Chem.* **1912**, 394, 111; b) M. Grzybowski, K. Skonieczny, H. Butenschon, D. T. Gryko, *Angew. Chem. Int. Ed.* **2013**, 52, 9900; *Angew. Chem.* **2013**, 125, 10084; c) M. S. Little, S. G. Yeates, A. A. Alwattar, K. W. J. Heard, J. Raftery, A. C. Edwards, A. V. S. Parry, P. Quayle, *Eur. J. Org. Chem.* **2017**, 2017, 1694; d) M. Grzybowski, B. Sadowski, H. Butenschon, D. T. Gryko, *Angew. Chem. Int. Ed.* **2020**, 59, 2998; *Angew. Chem.* **2020**, 132, 3020; e) R. S. Jassas, E. U. Mughal, A. Sadiq, R. I. Alsantali, M. M. Al-Rooqi, N. Naeem, Z. Moussa, S. A. Ahmed, *RSC Adv.* **2021**, 11, 32158.
- [15] a) M. Kastler, J. Schmidt, W. Pisula, D. Sebastiani, K. Müllen, *J. Am. Chem. Soc.* **2006**, 128, 9526; b) D. Lungerich, O. Papaianina, M. Feofanov, J. Liu, M. Devarajulu, S. I. Troyanov, S. Maier, K. Amsharov, *Nat. Commun.* **2018**, 9, 4756; c) J. Hieulle, E. Carbonell-Sanromà, M. Vilas-Varela, A. García-Lekue, E. Guitián, D. Peña, J. I. Pascual, *Nano Lett.* **2018**, 18, 418; d) X.-Y. Wang, X. Yao, A. Narita, K. Müllen, *Acc. Chem. Res.* **2019**, 52, 2491.
- [16] a) M. Rickhaus, M. Mayor, M. Juríček, *Chem. Soc. Rev.* **2017**, 46, 1643; b) I. R. Márquez, S. Castro-Fernández, A. Millán, A. G. Campaña, *Chem. Commun.* **2018**, 54, 6705; c) S. H. Pun, Q. Miao, *Acc. Chem. Res.* **2018**, 51, 1630; d) M. A. Majewski, M. Stepień, *Angew. Chem. Int. Ed.* **2019**, 58, 86; *Angew. Chem.* **2019**, 131, 90; e) G. Bati, D. Csókás, T. Yong, S. M. Tam, R. R. S. Shi, R. D. Webster, I. Pápai, F. García, M. C. Stuparu, *Angew. Chem. Int. Ed.* **2020**, 59, 21620; *Angew. Chem.* **2020**, 132, 21804; f) S. Matsubara, Y. Koga, Y. Segawa, K. Murakami, K. Itami, *Nat. Catal.* **2020**, 3, 710; g) M. C. Stuparu, *Acc. Chem. Res.* **2021**, 54, 2858; h) Chaolumen, I. A. Stepek, K. E. Yamada, H. Ito, K. Itami, *Angew. Chem. Int. Ed.* **2021**, 60, 23508; *Angew. Chem.* **2021**, 133, 23700; i) Y. Zhang, S. H. Pun, Q. Miao, *Chem. Rev.* **2022**, 122, 14554.
- [17] a) P. J. Evans, J. Ouyang, L. Favereau, J. Crassous, I. Fernández, J. Perles, N. Martín, *Angew. Chem. Int. Ed.* **2018**, 57, 6774; *Angew. Chem.* **2018**, 130, 6890; b) D. Reger, P. Haines, K. Y. Amsharov, J. A. Schmidt, T. Ullrich, S. Bönsch, F. Hampel, A. Görling, J. Nelson, K. E. Jelfs, D. M. Guldi, N. Jux, *Angew. Chem. Int. Ed.* **2021**, 60, 18073; *Angew. Chem.* **2021**, 133, 18221; c) X. Xiao, S. K. Pedersen, D. Aranda, J.

- Yang, R. A. Wiscons, M. Pittelkow, M. L. Steigerwald, F. Santoro, N. J. Schuster, C. Nuckolls, *J. Am. Chem. Soc.* **2021**, *143*, 983.
- [18] a) T. Horibe, S. Ohmura, K. Ishihara, *J. Am. Chem. Soc.* **2019**, *141*, 1877; b) P. Rempala, J. Kroulik, B. T. King, *J. Org. Chem.* **2006**, *71*, 5067; c) L. Zhai, R. Shukla, S. H. Wadumethrige, R. Rathore, *J. Org. Chem.* **2010**, *75*, 4748.
- [19] a) P. Rempala, J. Kroulik, B. T. King, *J. Am. Chem. Soc.* **2004**, *126*, 15002; b) Chaolumen, M. Murata, A. Wakamiya, Y. Murata, *Angew. Chem. Int. Ed.* **2017**, *56*, 5082; *Angew. Chem.* **2017**, *129*, 5164.
- [20] a) L. Zhai, R. Shukla, R. Rathore, *Org. Lett.* **2009**, *11*, 3474; b) M. A. Alsharif, Q. A. Raja, N. A. Majeed, R. S. Jassas, A. A. Alsimatee, A. Sadiq, N. Naeem, E. U. Mughal, R. I. Alsantali, Z. Moussa, S. A. Ahmed, *RSC Adv.* **2021**, *11*, 29826.
- [21] a) X. Dou, X. Yang, G. J. Bodwell, M. Wagner, V. Enkelmann, K. Müllen, *Org. Lett.* **2007**, *9*, 2485; b) J. L. Ormsby, T. D. Black, C. L. Hilton, Bharat, B. T. King, *Tetrahedron* **2008**, *64*, 11370; c) S. Nobusue, K. Fujita, Y. Tobe, *Org. Lett.* **2017**, *19*, 3227; d) Q. Miao, *Nat. Chem. Rev.* **2021**, *5*, 602; e) Z. Qiu, S. Asako, Y. Hu, C. W. Ju, T. Liu, L. Rondin, D. Schollmeyer, J. S. Lauret, K. Müllen, A. Narita, *J. Am. Chem. Soc.* **2020**, *142*, 14814; f) N. Ponugoti, V. Pathasarathy, *Chem. Eur. J.* **2022**, *28*, e202103530.
- [22] a) F. Ammon, S. T. Sauer, R. Lippert, D. Langerich, D. Reger, F. Hampel, N. Jux, *Org. Chem. Front.* **2017**, *4*, 861; b) J. Liu, A. Narita, S. Osella, W. Zhang, D. Schollmeyer, D. Beljonne, X. Feng, K. Müllen, *J. Am. Chem. Soc.* **2016**, *138*, 2602.
- [23] a) M. Krzeszewski, P. Świder, L. Dobrzycki, M. K. Cyrański, W. Danikiewicz, D. T. Gryko, *Chem. Commun.* **2016**, *52*, 11539; b) Y. Han, Z. Xue, G. Li, Y. Gu, Y. Ni, S. Dong, C. Chi, *Angew. Chem. Int. Ed.* **2020**, *59*, 9026; *Angew. Chem.* **2020**, *132*, 9111; c) G. González Miera, S. Matsubara, H. Kono, K. Murakami, K. Itami, *Chem. Sci.* **2022**, *13*, 1848.
- [24] J. Urieta-Mora, M. Krug, W. Alex, J. Perles, I. Fernández, A. Molina-Ontoria, D. M. Guldi, N. Martín, *J. Am. Chem. Soc.* **2020**, *142*, 4162.
- [25] J. M. Fernández-García, P. J. Evans, S. Medina Rivero, I. Fernández, D. García-Fresnadillo, J. Perles, J. Casado, N. Martín, *J. Am. Chem. Soc.* **2018**, *140*, 17188.
- [26] Y. Zhu, X. Guo, Y. Li, J. Wang, *J. Am. Chem. Soc.* **2019**, *141*, 5511.
- [27] Y. Zou, Y. Han, S. Wu, X. Hou, C. H. E. Chow, J. Wu, *Angew. Chem. Int. Ed.* **2021**, *60*, 17654; *Angew. Chem.* **2021**, *133*, 17795.
- [28] a) B. T. King, J. Kroulik, C. R. Robertson, P. Rempala, C. L. Hilton, J. D. Korinek, L. M. Gortari, *J. Org. Chem.* **2007**, *72*, 2279; b) H.-W. Ip, H.-F. Chow, D. Kuck, *Org. Chem. Front.* **2017**, *4*, 817; c) X.-Q. Sun, W.-S. Wong, Y. Li, D. Kuck, H.-F. Chow, *Org. Chem. Front.* **2021**, *8*, 5837; d) S. H. Pun, K. M. Cheung, D. Yang, H. Chen, Y. Wang, S. V. Kershaw, Q. Miao, *Angew. Chem. Int. Ed.* **2022**, *61*, e202113203; *Angew. Chem.* **2022**, *134*, e202113203.
- [29] a) S. Liu, D. Xia, M. Baumgarten, *ChemPlusChem* **2021**, *86*, 36; b) X. Zhang, Z. Xu, W. Si, K. Oniwa, M. Bao, Y. Yamamoto, T. Jin, *Nat. Commun.* **2017**, *8*, 15073.
- [30] P. Izquierdo-García, J. M. Fernández-García, I. Fernández, J. Perles, N. Martín, *J. Am. Chem. Soc.* **2021**, *143*, 11864.
- [31] Z. Chen, C. S. Wannere, C. Corminboeuf, R. Puchta, P. v. R. Schleyer, *Chem. Rev.* **2005**, *105*, 3842.
- [32] For a related aromaticity gain in anthracene derivatives, see: Y. García-Rodeja, I. Fernández, *Chem. Eur. J.* **2017**, *23*, 6634.

Manuscript received: October 24, 2022

Accepted manuscript online: December 10, 2022

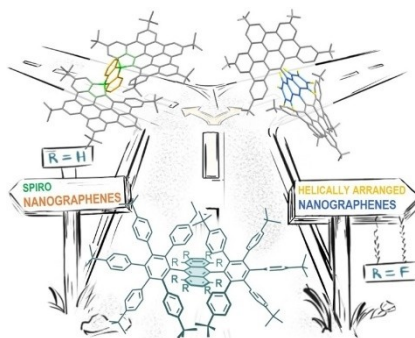
Version of record online: ■■■, ■■■

Research Articles

Nanographenes

P. Izquierdo-García, J. M. Fernández-García,
J. Perles, I. Fernández,*
N. Martín* **e202215655**

Electronic Control of the Scholl Reaction:
Selective Synthesis of Spiro vs Helical
Nanographenes



The electronic nature of the starting substrate decides the fate of the reaction: Anthracene-based polyphenylenes lead to less-known spiro ($R=H$) or helical ($R=F$) nanographenes under mild Scholl conditions, depending upon the substitution pattern on the anthracene core. DFT calculations reveal that the formation, or not, of the trityl cation is the key issue.